Invited Articles

# Dynamics of bubbles and ultrasound: Diagnostic imaging to blood pressure monitoring and tissue engineering

Kausik Sarkar
*Department of Mechanical and Aerospace Engineering, The George Washington University, Washington, DC 20052, USA*

(Received 22 July 2024; accepted 21 October 2024; published 17 March 2025)

Coated microbubbles in conjunction with ultrasound have emerged as an important biomedical tool for diagnostic imaging and therapeutics. Here, I offer my perspective based on research spanning over two decades, highlighting the underlying physics of linear and nonlinear bubble dynamics. I will describe our effort at mathematical modeling of contrast microbubble behaviors, specifically our adoption of an interfacial rheological model for the stabilizing shell and a hierarchical approach of model building and improvement using attenuation and scattering experiments. I will describe our collaborative effort at using the sensitivity of the acoustic response of microbubbles to ambient hydrostatic pressure for a subharmonic aided pressure estimation (SHAPE) method for noninvasive organ-level blood pressure monitoring. Other collaborative projects demonstrated microbubbles together with low-intensity pulsed ultrasound (LIPUS) to be an effective tool in tissue engineering, growing bone and cartilage from human mesenchymal stem cells in a 3D printed tissue engineering scaffold. We have theoretically investigated various underlying mechanisms for such bioeffects of ultrasound-insonated microbubbles, specifically microstreaming at low acoustic excitations and cavitating jet formation at high excitations for shelled microbubbles. Finally, I briefly describe my computational research on viscous and viscoelastic emulsions and suspensions of drops, vesicles, and biological cells.

DOI: 10.1103/PhysRevFluids.10.030501

## I. BUBBLES AND SOUND

My journey into the fascinating world of bubbles began in 1990 when I started my PhD at Johns Hopkins University under the guidance of Professor Andrea Prosperetti, one of the foremost experts on bubble dynamics. At the time, his group was investigating underwater sound propagation and acoustic scattering from oceanic bubble clouds, specifically their roles in the production and scattering of low-frequency sound [1,2]. My dissertation had two parts: the first part was on the acoustics of oceanic bubbles and their clouds [3,4], and the second on transport processes on rough surfaces [5,6]. The acoustic part of the thesis formulated a theory of coherent and incoherent scattering from bubbles giving rise to a homogeneous bubbly medium with a characteristic sound speed, and acoustic scattering from bubble clouds of different shapes at the ocean surface. I became familiar with individual bubble dynamics governed by the celebrated Rayleigh-Plesset (RP) equation (Milton Plesset was the PhD advisor of Andrea at Caltech) describing the time evolution of the radius $R(t)$ of a spherical bubble:

$$\rho\left(R\ddot{R}+\frac{3}{2}\dot{R}^2\right)=\left(p_0+\frac{2\gamma}{R}\right)\left(\frac{R_0}{R}\right)^{3k}-\frac{2\gamma}{R}-4\mu\frac{\dot{R}}{R}-p_0+p_a, \tag{1}$$

Contact author: sarkar@gwu.edu

 

where $R_0$ is the initial bubble radius, $\rho$ is the surrounding liquid density, $\mu$ is the liquid viscosity, and $p_0$ is the ambient pressure, which initially (at rest) is lower than the inside bubble pressure $P_G$ due to the Laplace pressure caused by surface tension $\gamma$ [i.e., $P_G(t=0) = p_0 + 2\gamma/R_0$]. The bubble undergoes a volume oscillation following a gas law with a polytropic constant $k$, while driven by an acoustic pressure $p_a$. The RP equation (best thought of as Newton's second law) can be obtained by integrating the Navier-Stokes equation with the spherical velocity $u(r,t) = R^2\dot{R}/r^2$ and noting that the pressure at the bubble interface on the liquid side is given by the normal stress jump condition [7] as

$$p(R,t) = P_G - \frac{2\gamma}{R} - 4\mu\frac{\dot{R}}{R} = \left(p_0 + \frac{2\gamma}{R}\right)\left(\frac{R_0}{R}\right)^{3k} - \frac{2\gamma}{R} - 4\mu\frac{\dot{R}}{R}. \tag{2}$$

The nonlinear equation shows that a bubble is capable of both a linear response at low excitation and responses containing frequency components other than one at the excitation frequency (they play a critical role in nonlinear imaging modalities with high signal-to-noise ratio) when driven hard with a strong excitation. Upon linearization, the RP Eq. (1) simplifies to a simple harmonic oscillator for the radius deviation $X = R(t) - R_0$ under a sinusoidal forcing, $p_A(t) = P_A \sin(\omega t)$:

$$\ddot{X} + \frac{\dot{X}}{\rho R_0^2}(4\mu) + \frac{X}{\rho R_0^2}\left[3kP_0 + \frac{2\gamma}{R_0}(3k-1)\right] = \frac{P_A}{\rho R_0}\sin\omega t, \tag{3}$$

with a characteristic resonance frequency

$$f_0^{\text{free bubble}} = \frac{1}{2\pi R_0}\sqrt{\frac{1}{\rho}\left(3kp_0 + \frac{2\gamma}{R_0}(3k-1)\right)}, \tag{4}$$

demonstrating that the "spring constant" of the oscillator derives from the compressible gas core (the pressure inside) and the "mass" term is that of the surrounding liquid (not that of the gas inside or the bubble shell). Note that very often the well-known Minneart formula for the resonance frequency,

$$f_{\text{Minneart}}(\text{MHz}) \approx \frac{3.26}{R_0(\mu\text{m})},$$

of a free bubble has caused confusion in the contrast agent literature. The formula is appropriate for bubbles of size millimeters and above; it includes only the term due to the gas compressibility—the first term inside the brackets in Eq. (4)—and neglects the contribution due to surface tension which is not negligible for micron-size contrast microbubbles [8].

## II. MICROBUBBLES AS CONTRAST-ENHANCING AGENTS FOR ULTRASOUND IMAGING

Although ultrasound as a biomedical imaging modality is well known, using bubbles for medical ultrasound imaging is a relatively recent phenomenon. It was a serendipitous discovery by Gramiak and Sha [9] that an agitated saline solution when injected into the left ventricle produced strong echoes of the aorta due to air bubble activity created by the agitation. I too came to know of bubbles being used in ultrasound imaging by an accident in 2001. I was finishing up my postdoctoral studies with Bill Schowalter, then the Dean of Engineering at the University of Illinois at Urbana Champaign (UIUC), working not on bubbles but on direct numerical simulations of viscous and viscoelastic drops in various flows. Ken Watkin, a professor of Speech and Hearing Science at UIUC, who also ran an ultrasound imaging clinic, met Bill at a social event and casually asked him (I was told, over a glass of wine effervescent with bubbles) if he knew anything about bubbles. Because of my thesis background, Bill pulled me in for a joint meeting, which changed my life forever.

For the first time, I came to know that microbubbles in the diameter range of 1–10 μm are being used as contrast-enhancing agents for medical ultrasound imaging. Because of the compressible gas core, bubbles have several orders of magnitude higher scattering cross sections (ability to reflect

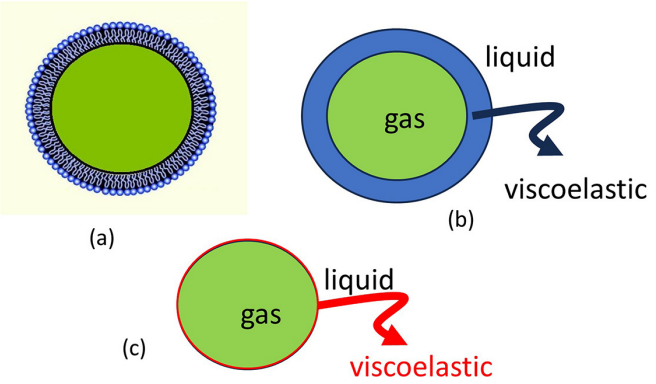


FIG. 1. (a) Amphiphilic molecules with a hydrophilic head and a hydrophilic tail self-assembled on the gas-liquid interface of the microbubble forming a shell. The surface-active molecules reduce the surface tension stabilizing against Laplace pressure-driven dissolution. It also hinders gas permeability through the interface. The stabilizing encapsulation modeled as (b) a thick viscoelastic shell characterized by bulk material properties such as viscosity and elasticity, and as (c) an infinitesimally thin interface with intrinsic rheology characterized by interfacial material properties such as surface tension, interfacial viscosity, and interfacial elasticity.

sound) than a particle or droplet of similar size, which is responsible for their outsize effects in all phenomena involving bubbles and generates a strong echo in an ultrasound image.

A micrometer-diameter air bubble is inherently unstable due to rapid dissolution driven by the high Laplace pressure $2\gamma/R$, which as we noted, is significant for its small size [10]. The stability of gas bubbles due to outward gas diffusion was originally modeled by Epstein and Plesset [11] showing that a micrometer-size air bubble lasts only for tens of milliseconds [12–14]. Bubbles after being introduced by an intravenous injection take tens of minutes to reach the heart. To enhance their lifetime, contrast microbubbles are stabilized by replacing the air with higher molecular weight perfluorocarbon (PFC) gas [such as perfluorobutane (PFB) or $SF_6$] and by endowing them with an encapsulating shell made of surface-active molecules such as lipids, proteins, or other surfactants. The amphiphilic nature of the molecules leads them to spontaneously self-assemble into a monolayer at the interface [Fig. 1(a)]. One of the first formulations of microbubbles, designed for contrast ultrasound, was Albunex (Molecular Biosystems Inc., SanDiego, CA, USA), an air bubble encapsulated by human serum albumin, approved in the USA in 1993 for left ventricle studies. Its formulation was later improved by replacing the air with a PFB core, resulting in the first second-generation contrast agent, Optison (GE Healthcare, Oslo, Norway), approved by the FDA in 1997. The PFC core extended the lifespan of contrast microbubbles to several minutes, while the shell took it to hours [12]. Albunex and Optison were followed by others such as Levovist (Schering AG, Germany), Definity (Lantheus Medical Imaging Inc., North Billerica, MA), Sonazoid (GE Healthcare, Oslo, Norway), and Sonovue (Bracco, Princeton, NJ), all of them encapsulated with different lipid shells. Over the years, microbubbles have found applications also in drug and gene delivery and therapeutics [15–17].

## III. ENCAPSULATING SHELL OF A CONTRAST MICROBUBBLE

The research on contrast microbubbles was initiated by clinical practitioners and physical scientists associated with clinical facilities building upon the large existing literature on free bubble dynamics and cavitation. Some of the initial pioneering studies were spearheaded by de Jong and co-workers [18–22] in the 1990s. It was clear from the beginning that the shell plays a critical role in the competing requirements of extended lifetimes and stronger echoes. Early efforts at modeling the shell rightly identified two additional shell contributions—one springlike and the

other a damper—to the damped oscillator underlying a microbubble response. The pioneering model by de Jong and co-workers added shell elasticity ($S_p$) and friction ($S_F$) factors to the RP equation (1) [19]. Other models have been used to investigate and analyze contrast microbubble behaviors [18–20,23–28]. The first rigorous model of a shell was attempted by noted acoustician, Charlie Church, who treated the shell as a "finite-thickness layer" of rubbery material [Fig. 1(b)] characterized by a constitutive equation containing bulk elasticity modulus and viscosity [27] performing a nice perturbative analysis of the model without relating it to a specific contrast agent, only to be modified by Hoff *et al*. [29] and applied to investigate *in vitro* experiments involving various contrast agents.

This is when I started my first faculty position at the University of Delaware (UD) and decided to devote a substantial part of my new research effort to contrast agents. I am also fortunate for a chance contact with the Radiology Department of Thomas Jefferson University (TJU), particularly the collaboration (continuing after two decades) with Professor Flemming Forsberg which provided the all-important clinical relevance to our research. I also started an experimental laboratory which was deemed an extremely risky venture for a starting tenure track assistant professor with no prior background in experiment. I am greatly indebted to my first postdoctoral scientist, Dr. Dhiman Chatterjee, currently a professor at IIT Madras, for getting me started on this path. I continue to have more than 50% of my research in experiments today.

Our first contribution was the proposal of an interfacial model in contrast to the above "finite-thickness-layer model" (Fig. 1). We identified that a finite-thickness-layer model with bulk constitutive material properties might not be appropriate for a monolayer, or at most a few-molecule-thick layer, and the cartoon rendering of the bubble interface decorated by amphiphilic molecules does a disservice to the reality of the wide length scale separation between the few-angstrom thickness of the shell and the overall micrometer size of the bubble [Fig. 1(a)] giving rise to the finite-thickness layer model [Fig. 1(b)]. In reality, in the scale of the bubble the shell is an infinitesimally thin interface indicated by the red line in Fig. 1(c).

## IV. INTERFACIAL RHEOLOGICAL MODELS FOR SHELL: HIERARCHICAL APPROACH TO MODELING

Arguing above, we proposed in 2003 an interfacial rheological model for the encapsulating shell of a contrast microbubble [30] with interfacial elasticity and interfacial viscosity in contrast to their bulk counterparts (Fig. 1). Such modeling has since become a standard approach in contrast agent literature [7,31–33]. It indicates a constitutive relationship between the interfacial stress $\boldsymbol{\tau}_s(\boldsymbol{\varepsilon}_s; \gamma, E^s, \kappa^s)$ and the interfacial strain $\boldsymbol{\varepsilon}_s$ characterizing the shell with interfacial material properties, such as surface tension $\gamma$, interfacial elasticity $E^s$, and interfacial viscosity $\kappa^s$. These material properties along with the appropriate model are crucial for the optimization of microbubble behavior for a specific clinical application.

Constitutive modeling is traditionally beset with the problem of how to choose the most appropriate one from a class of models with increasing complexity and parameters, which are hard to measure by experiments. We have adopted a hierarchical approach to modeling the shell, starting with the simplest model with few parameters, and progressively modifying them as warranted by experimental findings. Once a model is chosen, the model parameters specific to a contrast microbubble were determined using experimentally measured attenuation [34] through a suspension of microbubbles, and then validating the model against a second independent experiment, namely, linear and nonlinear scattered responses from the microbubble (Fig. 2). The nonlinear responses, such as the second and subharmonic signals, are generated only by the microbubbles, giving rise to novel imaging modalities such as harmonic imaging with higher contrast-to-tissue ratio differentiating the target area from the surrounding tissues [35,36]. We will see below that the subharmonic response plays a critical role in noninvasive organ-level pressure estimation [37–40]. In the following, we describe our effort at this hierarchical model building resulting in increasingly more complex models over a decade.

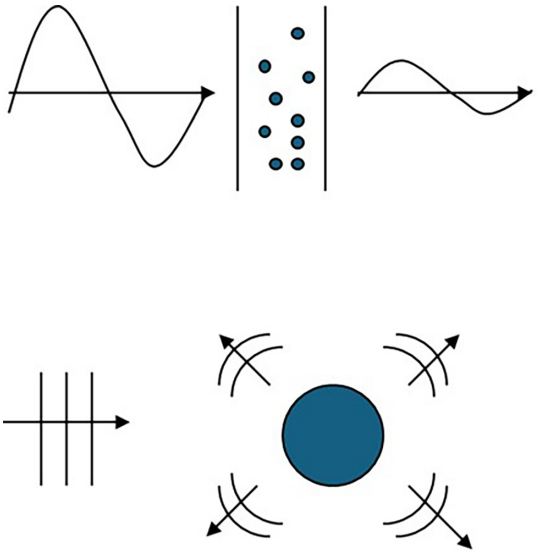

FIG. 2. Attenuation of an ultrasound wave passing through a layer of microbubbles leading to an attenuated wave (top). Scattering of a plane wave by microbubbles results in radially outgoing scattered signals.

### A. Newtonian model (2003) [30]

In our first-ever paper on contrast microbubbles, we proposed a simple rheology—a Newtonian interface with a dilatational viscosity ($\kappa^s$) and a surface tension ($\gamma_0$):

$$\gamma(R) = \gamma_0(\text{constant}) \quad \text{and} \quad \kappa^s(R) = \kappa^s(\text{constant}). \tag{5}$$

The bubble surface dilatation $A^{-1}dA/dt = 2\dot{R}/R$ ($A = 4\pi R^2$) results in an additional tension $2\kappa^s\dot{R}/R$ changing (2) to

$$p(R,t) = \left(p_0 + \frac{2\gamma}{R_0}\right)\left(\frac{R_0}{R}\right)^{3k} - \frac{2\gamma_0}{R} - \frac{4\kappa^s\dot{R}}{R^2} - 4\mu\frac{\dot{R}}{R}. \tag{6}$$

The resulting model was used to compute the extinction cross section $\sigma_e(R_0,\omega)$ of a bubble, the amount of energy lost due to a bubble in the path of an incoming acoustic wave. It is integrated over the bubble population to obtain the attenuation coefficient $\alpha(\omega)$, which is the exponential constant characterizing the decrease of the acoustic intensity $I(x)$ through a length $x$ of the suspension of contrast microbubbles:

$$\alpha(\omega)\ (\text{in dB}) = 10\log_{10}e\int_{R_{0\,\min}}^{R_{0\,\max}}\sigma_e(R_0,\omega)n(R_0)dR_0, \quad (\omega;x) = I(\omega;0)e^{-\alpha x}. \tag{7}$$

Implicit in the frequency-dependent attenuation expression is an assumption that every frequency component propagates and attenuates independently without nonlinear energy transfer from other frequencies; the underlying strong linearity is often missed in the attenuation description in the literature [34,41]. The attenuation is based on the linearized RP equation (3) (modified for the Newtonian model) with a simple harmonic motion structure with a resonance frequency and a damping term comprising contributions from the liquid, shell, and reradiation:

$$\begin{aligned}\delta_{\text{total}} &= \delta_{\text{liquid}} + \delta_{\text{interface}} + \delta_{\text{radiation}},\\ \delta_{\text{liquid}} &= \frac{4\mu}{\rho\omega_0 R_0^2}, \quad \delta_{\text{interface}} = \frac{4\kappa^s}{\rho\omega_0 {R_0}^3}, \quad \delta_{\text{radiation}} = \frac{\omega^2 R_0}{\omega_0 c},\end{aligned} \tag{8}$$

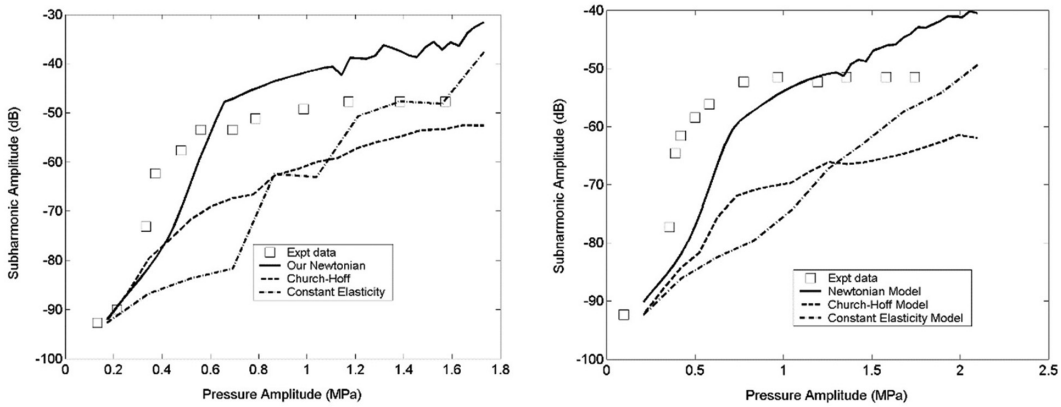


FIG. 3. Measured and predicted subharmonic scattered response according to the Newtonian, constant elasticity, and Church-Hoff models at 3 MHz (left) and 4 MHz (right) excitation frequencies. Note that the Newtonian model, even with an unphysically high surface tension value, matches the experiments better than the constant elasticity viscoelastic model.

where $c$ is the sound speed in the liquid. [Note the reradiation damping is added separately here as warranted by the incompressible RP equation (1); a suitable modification of the RP equation accounting for compressibility automatically obtains it (see our previous publication [31] for additional details)]. The damping term gives rise to the frequency-dependent extinction cross section:

$$\sigma_e(R_0, \omega) = 4\pi R_0^2 \frac{c\delta_{\text{total}}}{\omega_0 R_0} \frac{\Omega^2}{\left[(1-\Omega^2)^2 + \Omega^2 \delta_{\text{total}}^2\right]}, \quad \Omega = \frac{\omega}{\omega_0}. \tag{9}$$

The rheological parameters such as $\gamma_0$ and $\kappa^s$ specific to a contrast agent were determined using the measured attenuation $\alpha(\omega)$ by minimizing the error $\text{Er}(\gamma, \kappa^s, \ldots) = \sum_i [\alpha(\omega_i) - \alpha^{\text{meas}}(\omega_i)]^2$ between the measured attenuation and the model attenuation. The model prediction was validated using the linear and nonlinear (components at frequencies other than of excitation) scattered responses from the outgoing scattered pressure from a microbubble:

$$P_s(r,\, t) = \rho \frac{R}{r}(2\dot{R}^2 + R\ddot{R}). \tag{10}$$

This article introduced the dilatational viscosity $\kappa^s$ in the contrast agent literature in 2003 and measured it by obtaining $\kappa^s \sim (5\text{–}8) \times 10^{-8}$ N s. Since then, many measurements have obtained the same order values for $\kappa^s$ for many contrast agents. However, our procedure resulted in surface tension values of $\gamma_0 \sim 0.7\text{–}0.9$ N/m for the coated microbubbles, one order of magnitude higher than the value (0.07 N/m) at the air-water interface. The contrast microbubbles are coated with surface-active amphiphilic molecules to stabilize them against dissolution by reducing the surface tension. Even though this Newtonian model (NM) was able to match with the experimentally measured subharmonic response from Fig. 3 in our proposed validation effort, the unreasonably high surface tension values signaled that the model needed modification, specifically an elastic component for the encapsulation rather than a constant surface tension.

### B. Linear viscoelastic model (constant elasticity; 2005) [7]

The above concern led us to propose a linear viscoelastic shell model in 2005, where instead of constant surface tension, an interfacial elasticity $E^s$ (also known as the Gibbs elasticity) was introduced as a derivative of the surface tension with respect to the area fraction $dA/A$ [relative to an area with reference radius $R_E$, $(R^2 - R_E^2)/R_E^2$], leading to three characteristic parameters, $\gamma_0$, $\kappa^s$,

and $E^s$:

$$\gamma(R) = \gamma_0 + E^s\left(\frac{dA}{A}\right) = \gamma_0 + E^s\left[\left(\frac{R}{R_E}\right)^2 - 1\right], \quad \kappa^s(R) = \kappa^s(\text{constant}), \tag{11}$$

Note that unlike the NM, where without excitation at rest the bubble has a larger pressure inside the bubble due to surface tension and therefore is susceptible to dissolution from gas diffusion, here a pressure equilibrium could be assumed at the initial radius $R_0$, which will be strained compared to $R_E = R_0(1 - \gamma_0/E^s)^{-1/2}$, the unstrained radius. The new model replaces the constant $\gamma_0$ of the NM with the new $\gamma(R)$ as given in (11) in Eq. (6). Also, the initial pressure equilibrium here replaces the first term on the right-hand side of (6), $p_0 + 2\gamma/R_0$, by $p_0$.

The same error minimization procedure as before is applied to find that this linear viscoelasticity model with a constant shell elasticity (hence also called constant elasticity or CEM model) obtains a reasonable value of the reference surface tension $\gamma_0 \sim 0.02$ N/m and $E^s \sim 0.55$ N/m for the Sonazoid bubble keeping the same value for $\kappa^s (\sim 10^{-8}$ N s) (one would not expect changing the elastic part of the model would affect the viscosity). However, in the validation step, it fails to match the subharmonic response severely underpredicting it (Fig. 3). We recognized that the linear model with a constant elasticity might be an inappropriate element while being demanded to describe the nonlinear subharmonic response present under large oscillations driven by stronger acoustic excitations.

### C. Nonlinear strain-softening model (exponential elasticity) [31]

This led us to propose in 2010 a nonlinear viscoelastic model where the surface elasticity was assumed to change with the surface area fraction exponentially softening its resistance with area increase leading to four characteristic parameters $\gamma_0$, $\kappa^s$, $E^s$, and the exponential folding parameter $\alpha$ :

$$\gamma(R) = \gamma_0 + E_0^s e^{-\alpha[(R/R_E)^2 - 1]}\left[\left(\frac{R}{R_E}\right)^2 - 1\right], \quad \kappa^s(R) = \kappa^s(\text{constant}). \tag{12}$$

Using the same procedure as above, one obtains for this model (called exponential elasticity or EEM) $\kappa^s \sim 10^{-8}$ N s, $\gamma_0 \sim 0.02$ N/m, $E^s \sim 0.55$ N/m. It succeeded in the validation test predicting the subharmonic response as well (Fig. 4).

These three articles spanning close to a decade describe our effort at progressive model building, first proposing an interfacial rheological model and adopting a two-pronged approach of using two independent experiments: one, attenuation, for finding the characteristic constitutive properties and the second, subharmonic scattering, for validating the model for its predictive ability. We started initially with a simple constitutive equation, progressively improving it over the years as warranted by experimental observations.

### D. Other interfacial rheological models

During this period, other models appeared in the literature [28,32,42–46], the most important among them being the Marmottant model. This model, published in the same journal 3 months [32] after our 2005 article on the linear viscoelastic model, introduced an interfacial elasticity in an identical way, as a derivative of the surface tension with respect to the area fraction but with critical additional innovations:

$$\gamma(R) = \begin{cases} 0 & \text{for } R \leqslant R_{\text{buckling}} \\ \chi\left(\frac{R^2}{R_{\text{buckling}}^2} - 1\right) & \text{for } R_{\text{buckling}} \leqslant R \leqslant R_{\text{rupture}} \text{ and } \kappa^s(R) = \kappa^s, \\ \gamma_w & \text{for } R \geqslant R_{\text{rupture}} \end{cases} \tag{13}$$

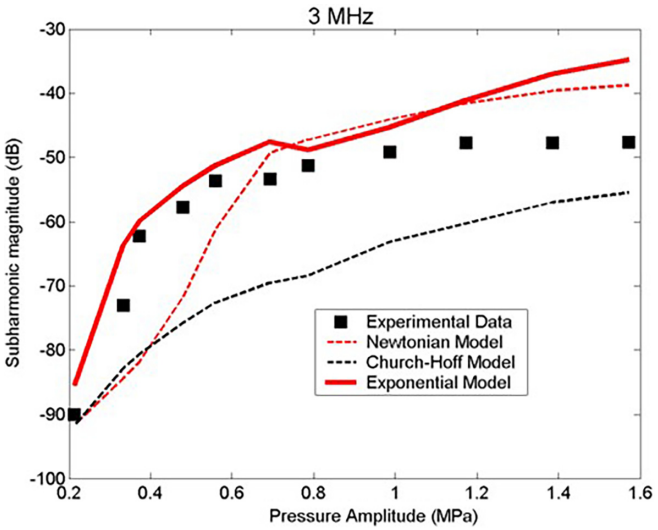


FIG. 4. Measured and predicted subharmonic scattered response from Sonazoid contrast agents according to the NM, Church-Hoff, and exponential models at 3 MHz excitation frequency.

where $\chi$ [same as $E^s$ in (11) in our model] is the elastic modulus of the shell. However, unlike our linear viscoelastic model, the linear regime here is limited between a buckling radius $R_{\text{buckling}} = R_0[1 + \gamma(R_0)/\chi]^{-1/2}$ below which the shell buckles with the surface tension becoming zero and a rupture radius $R_{\text{rupture}} = R_{\text{buckling}}[1 + \gamma_\omega/\chi]^{1/2}$, above which the shell ruptures, leaving a surface tension value of an air-water interface. Buckling of the shell plays a critical role in the bubble dynamics and its incorporation allowed the Marmottant model to correctly predict many important observations obtained by the same group from Twente and Erasmus using a high frame-rate optical setup (Bradaris) including the compression-only behavior [47]. The model has been widely used in the literature. Following the publication of the Marmottant model, we incorporated zero surface tension at buckling in our 2010 nonlinear viscoelastic model by introducing a non-negative surface tension version of our model. The exponential strain softening of the elasticity in our model is a smoother version of the rupture feature in the Marmottant model. Both models along with the quadratic elasticity (in contrast to the exponential elasticity) were compared in our 2010 JASA article obtaining similar results.

We have used Marmottant and our EEM models for other in-house and commercial contrast microbubbles [8,41,48–50]. We have been involved in a collaborative project with the TJU on the development of an ultrasound-based noninvasive estimation of organ-level internal pressure (see Sec. V). Accordingly, we determined how ambient pressure affected the interfacial dilatational elasticity and viscosity contrast microbubbles Definity [48] and Targestar-P [49].

## V. MAKING OUR OWN LIPID-COATED MICROBUBBLES AND DROPLETS

Initially, we performed our *in vitro* investigation on commercial contrast agents [48,49] or microbubbles from other labs [8] or commercial vendors. However, my two brilliant PhD students Krishna Nanda Kumar and Mitra Aliabouzar started the synthesis of coated microbubbles (as well as micro- and nanoliquid droplets) in our laboratory. I must admit that they forced me to start this venture (today I am extremely glad that they did) despite my extreme hesitation to enter the world of "too much chemical synthesis." We synthesized lipid-coated perfluorobutane microbubbles in our laboratory, which was characterized using our exponential elasticity model [50]. By systematically varying the concentration of PEGylated lipids in the synthesis of bubbles coated with

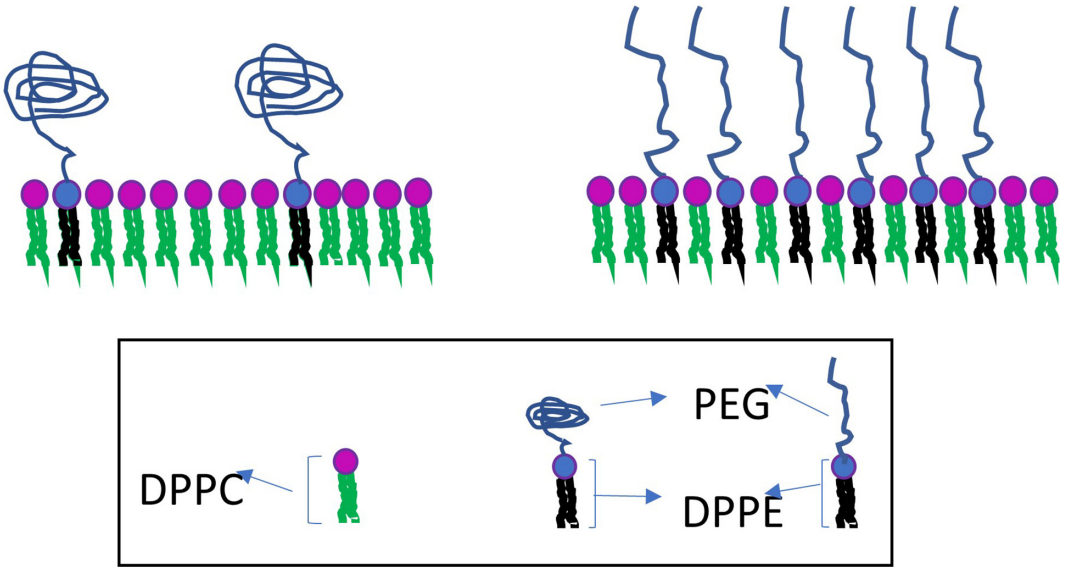


FIG. 5. Bubble encapsulation with a mixture of lipids (DPPC and Pegylated DPPE). At lower (higher) concentrations of Pegylated lipids, they assume a mushroom (brush) configuration changing the interfacial elasticity from 1.3 N/m in the mushroom region (at 2% and 5% PEG-DPPE) to 0.6 N/m in the brush region (10% and 20% PEG-DPPE).

DPPC (dipalmitoylphosphatidylcholine) and DPPE-PEG5000 (dipalmitoylphosphoethanolamine-polyethylene glycol-5000), we showed that, as higher concentrations lead to a transition of the PEGylated lipids from mushroom to brush configurations (Fig. 5), the shell dilatational elasticity correspondingly decreases significantly from $\sim$1.3 N/m for 2% and 5% of PEGylated lipid concentrations l to $\sim$0.6 N/m for 10% and 20% concentrations.

Mitra and Krishna performed an experimental investigation of acoustic droplet vaporization (ADV) explicating contradictory increasing and decreasing trends of ADV thresholds with frequency found in the literature. ADV is used for the *in situ* production of bubbles inside an organ by externally triggering vaporization using ultrasound [51,52].

I have offered a narrative describing some of the critical components of our experimental and modeling efforts and accomplishments. Modeling contrast microbubbles has often proved problematic due to the widely different results obtained for the same microbubbles arising due to the difference in bubble population even under similar synthesis protocol, or the vial-to-vial differences for the same commercial contrast agent, casting doubt on the robustness of a model and the characteristics properties for a particular contrast agent. This is somewhat mitigated by concentrating on single microbubble dynamics with a high frame-rate optical setup [25,53,54] or using monodisperse microbubbles [55,56]. However, even optical observations of single microbubble dynamics have led to different characteristic properties; e.g., widely different interfacial elasticity for identically prepared lipid-coated microbubbles, as we discussed in our previous work [41]. Currently, in collaboration with TJU, we are investigating the dynamics of monodisperse microbubbles.

## VI. GAS DIFFUSION, GROWTH, AND DISSOLUTION OF MICROBUBBLES

Microbubble contrast agents became viable with a sufficiently long lifetime within the body because of the low-solubility-gas (also called osmotic agent) core and the encapsulating shell which hinders their premature dissolution due to rapid gas diffusion. However, introducing low-solubility gases such as PFC also allows air diffusion into the bubble from the air-saturated liquid outside.

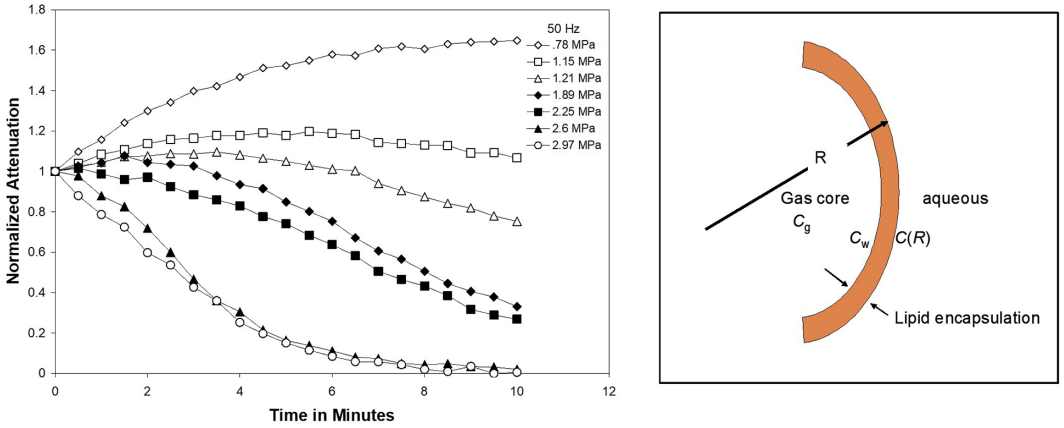


FIG. 6. Left: Variation of normalized attenuation with time under different acoustic pressure amplitudes for PRF (pulse repetition frequency) of 50 Hz. Right: Schematic of an encapsulated microbubble.

Kabalnov *et al*. [57,58] accounted for the simultaneous diffusion of air and an osmotic agent in the Epstein-Plesset dynamics to model the initial transient growth of a microbubble upon its introduction into a solution because of a rapid ingress of air from the surrounding liquid, and eventual dissolution due to a slow diffusion of PFC. The permeability hindering effect of the shell was modeled by assuming an additional diffusion resistance due to the shell in the Epstein-Plesset equation by a pioneering paper by Borden and Longo for single gas diffusion [51].

We were independently motivated by our investigation of Definity microbubble destruction under increasing acoustic excitations using the time-dependent total attenuation (Fig. 6) through a microbubble suspension [59]. At higher excitations, the attenuation decreased, independent of excitation strengths above a threshold excitation level, signaling shell destruction and subsequent rapid dissolution of the free air bubbles. However, at lower excitations, the attenuation was excitation dependent indicating acoustic effects on the dissolution, and at lowest excitations a transient increase due to the rapid air ingress into microbubbles from the surrounding medium.

It led us to model bubble dissolution [12] incorporating the shell hindrance effects rigorously into the diffusion model by proposing a boundary contribution at the bubble interface introducing a hindrance coefficient $h_g$ for the radial diffusion equation governing the gas concentration $C(r)$,

$$-k_g \left.\frac{\partial C}{\partial r}\right|_R = h_g[C_w - C(R)]. \tag{14}$$

Here $k_g$ is the gas diffusivity through the liquid. Other concentrations are defined in the Fig. 6 schematic. The coefficient $h_g$ accounts for mass flux through the encapsulation and can be thought of as $h_g \approx k_g^e/\delta_{\rm th}$, where $k_g^e$ is the diffusivity of the gas through the encapsulation and $\delta_{\rm th}$ is the thickness of the encapsulation. However, Fickian diffusion might be inappropriate for a monolayer encapsulation. An energy barrier model of gas permeation through the membrane would also give rise to (14) without a similar Fickian model for $h_g$ [51,60]. Solving the steady-state diffusion (radial Laplace) equation with this boundary condition in conjunction with the far-from-the-bubble gas concentration $C \to C(\infty)$, we obtain the monopole solution

$$C(r) = \frac{R^2[C_w - C(\infty)]}{r\left(\frac{k_g}{h_g} + R\right)} + C(\infty), \quad C_w = L_g C_g, \tag{15}$$

where the dissolved gas concentration $C_w$ in the shell in contact with the inside gas is related to the Ostwald coefficient $L_g$ and the inside gas concentration $C_g$, which in turn is determined by the gas

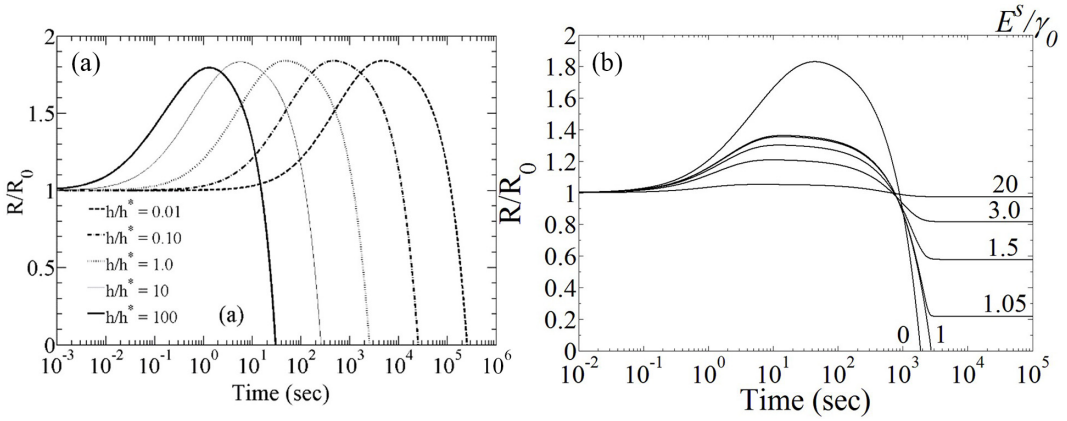


FIG. 7. (a) Growth and dissolution of a PFC microbubble for different permeability hindrance coefficients without an elastic shell $h_A^* = 2.857 \times 10^{-5}$m/s, $h_F^* = 1.6 \times 10^{-6}$m/s (other parameters are in [12]). (b) Same for different interfacial elasticity values. The bubble reaches stability for $E_s/\gamma_0 > 1$.

flux at the bubble wall

$$\frac{dm}{dt} = \frac{d}{dt}\left(\frac{4}{3}\pi R^3 C_g\right) = 4\pi R^2 k_g \left.\frac{\partial C}{\partial r}\right|_R \quad \text{or} \quad \frac{d(R^3 C_g)}{dt} = 3R^2 k_g \frac{[C(\infty) - L_g C_g]}{\left(\frac{k_g}{h_g} + R\right)}, \tag{16}$$

where (15) has been used. The gas concentrations are related to the gas law and the gas saturation level $f$ in the surrounding liquid [saturated ($f = 1$), undersaturated ($f < 1$), or oversaturated ($f > 1$)] to the local gas pressure:

$$C_g = \frac{1}{R_G T}\left(p_0 + \frac{2\gamma}{R}\right), \quad C(\infty) = \frac{f L_g p_0}{R_G T}. \tag{17}$$

$R_G$ is the gas constant and $T$ is the temperature. It leads to Eq. (16) becoming

$$\frac{dR}{dt} = -L_g \frac{1 - f + 2\gamma/(R p_{\text{atm}})}{\left(1 + \frac{4\gamma}{3R p_{\text{atm}}}\right)\left(\frac{1}{h_g} + \frac{R}{k_g}\right)}. \tag{18}$$

Firstly, it shows the *ad hoc* shell permeability resistance [51] $R_{\text{shell}} = 1/h_g$. Here the coefficient $h_g$ appears in the boundary condition of a rigorous boundary value problem for the gas diffusion. It also can be shown that the new boundary condition radically alters the analysis for the unsteady diffusion problem solved for free bubbles by Epstein-Plesset [11]. One cannot add in an *ad hoc* fashion the unsteady resistance term $k_g/\sqrt{\pi t}$ (appearing in the Epstein-Plesset solution) in the second multiplicative factor of the denominator in Eq. (18) as was done previously [51]. Equation (18) clearly shows the two effects driving dissolution for a free bubble—undersaturation $1-f$ and surface tension $\gamma$. A small $h_g$ (less permeable membrane) and small $L_g$ (low solubility) hinder bubble dissolution. In a gas-saturated ($f = 1$) medium, one can analytically integrate the equation to obtain a dissolution time in terms of $h_g R_0/k_g$ (an analog of the Sherwood number for convective mass transfer with $h_g$ being an analog of the convection coefficient):

$$\tilde{t}_{\text{diss}} \equiv \frac{t_{\text{diss}}}{R_0^2/k_g} = \frac{1}{L_g}\left[\frac{p_{\text{atm}} R_0}{\gamma}\left(\frac{1}{6} + \frac{k_g}{4h_g R_0}\right) + \frac{2k_g}{3h_g R_0} + \frac{1}{3}\right]. \tag{19}$$

We studied the growth and dissolution of a microbubble with a nonelastic shell [Fig. 7(a)]. In the limit of zero surface tension, Eq. (19) stabilizes an air bubble in an air-saturated medium. A zero surface tension can arise in a prestressed microbubble shell [see Eqs. (11) or (12)] as we saw in Sec. IV. We investigated the effects of shell elasticity [13] on growth and dissolution and found that the

bubble is stabilized by an elastic shell [Fig. 7(b)]. However, a bubble is only neutrally stable at zero surface tension (the state allowed after buckling in a shrinking Marmottant bubble; see Sec. IV) and only reaches true stability for negative compressive stress (i.e., for a negative surface tension) [14].

It must be admitted that the above effort at modeling the shell elasticity and shell permeability hindrance, although predicted transient growth and explained stability, we noticed that the observed timescale of the transient growth seen in Fig. 6 is large compared to what we find in the model further indicating a continuing need for further investigation. Currently, we are exploring effects such as decreasing permeability of a shrinking microbubble as the shell condenses which would increase the timescale of transient growth. There are additional complications of lipid shedding postbuckling being studied extensively by the Borden group [51,61,62].

## VII. NONINVASIVE PRESSURE ESTIMATION USING ULTRASOUND: SUBHARMONIC AIDED PRESSURE ESTIMATION (SHAPE)

Local organ-level pressure information can be a critical marker to determine the state of health and diagnose several diseases related to the heart and vascular system; e.g., portal hypertension [63,64], which is the underlying cause of most of the complications of cirrhosis and subsequent mortality [65,66]. Current techniques for organ-level pressure measurement are either invasive, such as catheter-based pressure transducers, which have to be introduced directly into the hepatic vasculature, or noninvasive but indirect and qualitative, such as using CT, MRI, or ultrasound imaging to diagnose liver cirrhosis (with accuracies of 64%–70%) [67]. For cardiac pressure measurement within the chambers, critical for the assessment and management of heart failure patients [68,69], the currently available noninvasive procedure of measuring pressure gradients across valves of the heart using Doppler ultrasound [70] has been reported to be nonreproducible [71,72].

We have been involved in a collaborative project with TJU in their effort to develop a microbubble-based noninvasive pressure monitoring technique. With several contrast agents, they found a strong reduction in subharmonic response with a rise in ambient pressure: a 25 kPa increase in pressure resulted in a 9.9 dB linear reduction in the peak amplitude of the subharmonic component for Levovist (Schering AG, Berlin, Germany) [73], 10.1 dB for Optison (GE Healthcare, Princeton, NJ), 11.03 dB for Definity (Lantheus Imaging, N. Billerica, MA), 12.2 dB for PRC-1 (Zhifuxian, Xinqiao Hospital, the Third Military Medical University, Chongqing, China), and 13.3 dB for Sonazoid [74]. It led the TJU group to propose a subharmonic aided pressure estimation (SHAPE) technique. SHAPE has been investigated in animal and human trials with promising results in measuring the left ventricular pressure [75], the interstitial fluid pressure in tumors [76,77], and portal hypertension in animals and humans [78–80].

In 2008, we were tasked by our TJU colleagues to numerically model the phenomenon for the optimization of SHAPE. Intuitively, one expects that an ambient pressure increase would decrease the bubble size and inhibit the oscillation of a microbubble and therefore would result in a reduced subharmonic response (as well as a reduction in the overall echo level) in conformity with the experimental observations noted above. Therefore, we were puzzled by our numerical simulation finding that increasing ambient pressure could either increase or decrease the subharmonic response in variance with the intuition [38]. We later demonstrated that the physical intuition was misleading, and both increasing and decreasing trends can be explained by investigating the underlying bubble dynamics.

We noted that increasing the ambient pressure increases the resonance frequency $f_0$ of the bubble [see Eq. (4) for free bubble, which would be appropriately modified for a coated bubble; the change in bubble radius $R_0$ due to increased ambient pressure was also accounted for], which in turn controls its subharmonic response. In fact, unlike other higher harmonics, the subharmonic response from a bubble is well known to be a threshold phenomenon, i.e., it appears only above a threshold excitation, the threshold being minimum at $f/f_0 \sim 2$ [81] (we have studied the effects of bubble models, specifically shell damping, on the minimum subharmonic threshold showing damping shifts the minimum form twice the resonance frequency to the resonance frequency [82,83]).

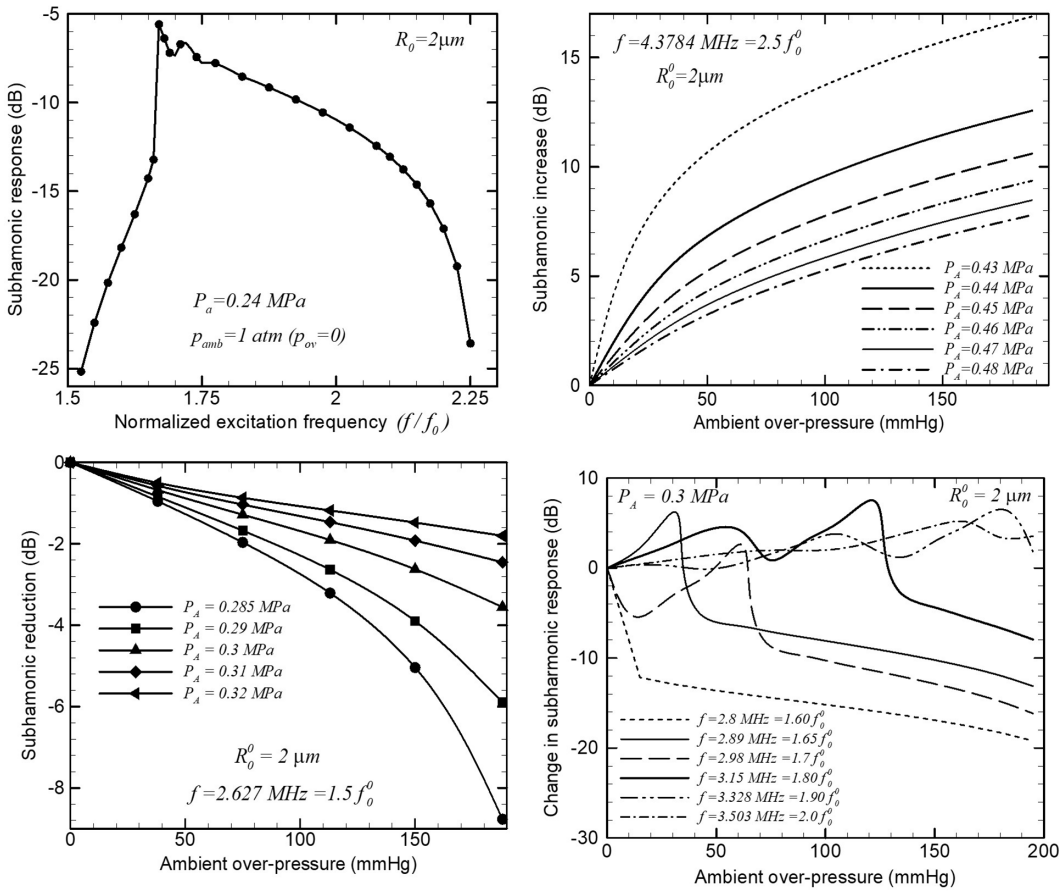


FIG. 8. (a) Subharmonic response from a microbubble as a function of frequency. (b) Positive correlation between subharmonic response and ambient pressure for an excitation frequency of 2.5 times the bubble's natural frequency (computed at ambient pressure). (c) Negative correlation between subharmonic response and ambient pressure for an excitation frequency of 1.5 times the bubble's natural frequency (computed at ambient pressure). (d) Nonmonotonic variation of the subharmonic response for excitation frequencies in a range of 1.6–2.0 times the natural frequency (computed at ambient pressure).

Correspondingly, one would expect, and we showed that just as resonance (i.e., when the excitation frequency $f$ matches the excitation frequency $f_0$) maximizes the fundamental response from a bubble, its subharmonic response reaches a maximum close to $f/f_0 \sim 2$ (where, as noted above, subharmonic threshold is minimum); for a 2-μm bubble at 0.24-MPa excitation amplitude, the maximum occurs around $f/f_0 \approx 1.65$ [Fig. 8(a)]. With $f/f_0$, it first increases until $f/f_0 > 1.6$, and above $f/f_0 > 1.8$ it decreases, and for the intermediate range $1.6 < f/f_0 < 1.8$, the subharmonic response varies in a nonsmooth way with $f/f_0$. We then showed that as we increase the ambient pressure, according to Eq. (4) $f_0$ increases and accordingly $f/f_0$ decreases, moving from right to left along the horizontal axis of Fig. 8(a). Therefore, as it approaches the subharmonic peak from the left, the subharmonic response increases with ambient pressure increase, as can be seen in Fig. 8(b) for $f/f_0^0 = 2.5$ ($f_0^0$, the resonance frequency at zero overpressure is used as a proxy for the resonance frequency $f_0$). Similarly, on the left side of the peak, an increase in ambient pressure decreases the subharmonic response [Fig. 8(c)], and for many intermediate values of $f/f_0$, we notice a nonmonotonic variation of the subharmonic response with ambient pressure [Fig. 8(d)].

Since our numerical findings, other groups also found that the subharmonic response decreases with ambient pressure for specific acoustic excitation parameters. The first such experimental finding of a subharmonic decrease with ambient pressure increases was by Frinking *et al*. [84] at a comparatively low excitation of 50 kPa. A detailed literature survey on experimental observations of both trends was presented in one of our recent articles [40]. We have recently performed *in vitro* experiments with our in-house lipid-coated PFB bubbles as well as commercially available bubbles delineating two different types of subharmonics, named type I at low excitations (less than $\sim$400 kPa), and type II at higher excitations. We found that often ambient pressure rise can lower the threshold of subharmonic generation, therefore triggering the type I subharmonic at higher ambient pressure while there was none at atmospheric pressure, resulting in a transient rising subharmonic trend. Type II, on the other hand, is the more traditional subharmonic one sees at higher excitations, which typically shows a marked decrease with ambient pressure [40]. In contrast, more complex pressurization-depressurization cycle-dependent behaviors were seen for SonoVue with $SF_6$ core bubbles due to the higher diffusivity of $SF_6$ compared to PFB [39]. We are continuing to investigate pressure-dependent subharmonic responses from different kinds of microbubbles with an aim to improve the sensitivity of SHAPE. Again, obtaining satisfactory models of observed bubble behaviors has proved difficult because of the various uncertainties discussed in Sec. IV.

## VIII. ULTRASOUND IN CONJUNCTION WITH MICROBUBBLES FOR BIOEFFECTS: CANCER THERAPY AND BONE AND CARTILAGE TISSUE ENGINEERING

Our effort at harnessing the bioeffects of ultrasound with or without microbubbles started at UD, again triggered by a chance event when the newly hired professor of the UD Biology department, Professor Randy Duncan, gave a seminar on the effects of hydrostatic pressure on bone cells, his research being motivated by bone loss experienced by astronauts in space. I was intrigued by the idea of replacing the static pressure stimulus with a periodically varying pressure of ultrasound. Randy was receptive to my idea of investigating the effects of ultrasound on bone cells. I had to convince Amit Katiyar, at that time my PhD student, to hurriedly learn cell culture in the Duncan laboratory, take our ultrasound setup there, and subject the cells to low-intensity pulsed ultrasound (LIPUS). Amit, whose thesis until then was primarily on numerical simulation of contrast microbubbles, to his credit, struggled against immense odds and produced results that LIPUS (0.5–5 MHz, 1–500 $mW/cm^2$) enhances the proliferation of MC3T3-E1 preosteoblast cells indicating a possible role of ultrasound in bone formation and fracture healing [85]. Once he got comfortable with cells and the Biology laboratory, we thought why not other cells? He performed a similar study for breast cancer cells T47D in the laboratory of Professor Krishna Pada Sarker finding that 10 min of LIPUS (1.5 MHz, 100 $mW/cm^2$) leads to a gradual decrease in cell numbers while not harming healthy MCF-12A breast cells (my PhD student Jenna Osborne at George Washington University helped finish this study; she took the initiative by collaborating with the GW Cancer Center laboratory and performed the MCF-12A study) [86].

After moving to George Washington University in 2011, I found an opportunity to continue my investigation of the bioeffects of ultrasound by collaborating with my departmental colleague Professor Grace Zhang. Professor Zhang's laboratory was involved in tissue engineering growing different tissues—bone, cartilage, and nerves—in the laboratory from human mesenchymal cells (hMSCs) in three-dimensional (3D) printed scaffolds. The hMSCs due to their pluripotency could differentiate into different cells in an appropriate biochemical environment. Our continuing collaboration over the years has helped establish the beneficial effects of ultrasound in conjunction with microbubbles in the proliferation and differentiation of hMSCs into different cells [87–91]. Not only do hMSCs increase in number when excited by ultrasound and more so in the presence of bubbles (Fig. 9), but they also showed a significant increase in the production of biomarkers for chondrogenesis, i.e., transformation into cartilage cells, chondrocytes, in the presence of LIPUS and microbubbles [88]. This study on chondrogenesis spearheaded by PhD student Mitra Aliabouzar in collaboration with the Zhang laboratory was followed by Jenna Osborne for osteogenesis from

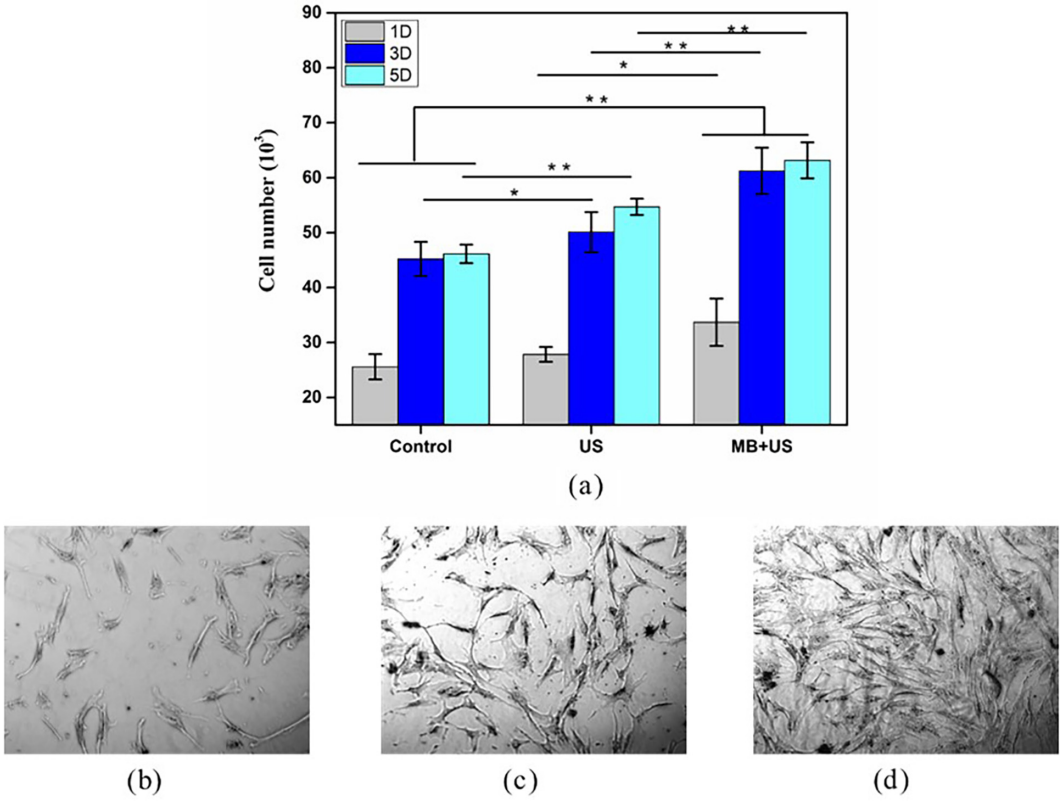


FIG. 9. (a) 1-, 3-, and 5-day hMSC proliferation with 3-min LIPUS (200 μs, 30 mW/cm$^2$, 1.5 MHz, 20% duty cycle) and 0.5% MB suspension. Microscopic images of hMSC growth 2 days after LIPUS (b) Control, (c) LIPUS, and (d) LIPUS with 0.5% (v/v) MB suspension. Values significantly different from the control group are indicated by * for $p < 0.05$ and ** for $p < 0.01$.

hMSCs, transformation into bone cells, in a similar 3D printed setup, showing a similar significant increase in osteogenic biomarkers [91].

Needless to say, these primarily experimental investigations of the cellular bioeffects of ultrasound and microbubbles studies were enabled by collaborations with Professor Duncan, Professor Sarker, and Professor Zhang. They were an interesting experience for a fluid mechanician, familiar with well-behaved systems of mechanics. It is exhilarating to be able to have an impact on important problems of medicine, and at the same time humbling and frustrating for the lack of understanding of the biochemical pathways underlying the experimental observations. I learned that such an approach is all too common in the complex world of biology.

### A. Mechanism behind the bioeffects of ultrasound and bubbles

Although the bioeffects of ultrasound-excited bubble activities noted above are induced through complex biochemical pathways, the pathways themselves are triggered by the mechanical stresses induced by the oscillations of acoustically excited microbubbles. Microbubbles could induce oscillating stresses in nearby fluids, microstreaming near a cell layer, or cavitate under high acoustic excitation forming violent oscillations and inertial jets. We have theoretically investigated them.

### 1. Acoustic microstreaming near a boundary

In addition to an oscillating flow, a vibrating body can also produce a steady streaming motion in the surrounding medium. The presence of a nearby boundary streaming motion due to an oscillating microbubble is named acoustic microstreaming [92–95]. It has been known to produce several beneficial and harmful bioeffects—hemolysis [96–98], sonoporation [88,99], drug delivery [100], and bone healing [85,87–89]—as well as in microfluidics transport [101], micromixing, and acoustic cleaning [102,103]. Lord Rayleigh first provided a theoretical explanation of the acoustic streaming observed in Kundt's tube as arising from the time-averaged nonlinear advection terms, $-\rho\langle \mathbf{u}^{(1)} \cdot \boldsymbol{\nabla} \mathbf{u}^{(1)} \rangle_t$ due to small oscillatory motion $\mathbf{u}^{(1)}$, acting as an inhomogeneous forcing term for the second-order equation of motion. It was followed in the 1950s by a series of pioneering studies [93,104,105] that strengthened its theoretical underpinning. Specifically, Nyborg [93] provided a generalized perturbative analysis of the streaming velocity near a boundary and offered expressions for the induced stresses under various conditions, which have been widely used in the literature. Most often an average expression of shear stress—$\mu u_L/\delta_{\rm bl}$, $\delta_{\rm bl} = \sqrt{\mu/\pi\rho f}$ is the Stokes boundary layer thickness and $u_L$ is the limiting streaming velocity at the edge of the boundary layer—was used. While looking at Nyborg's perturbative analysis, I underestimated his analytical power and casual neglect of many terms of the governing equations and thought that a more formal order analysis of the terms might result in an improved result. In the process of rederiving Nyborg's classical result, we computed the vertical velocity allowing streamlines of the vortex structure of the streaming flow along the wall for both free and coated microbubbles [106].

The perturbation method starts with an expansion of the velocity, $\mathbf{u} = \mathbf{u}^{(1)} + \mathbf{u}^{(2)} + \cdots$, and pressure, $p = p^{(1)} + p^{(2)} + \cdots$ in the approximation of a small amplitude oscillation of the order $\varepsilon R_0$, $\varepsilon \ll 1$ of a microbubble of radius $R_0$. The first-order approximation $\mathbf{u}^{(1)}$ solves the linearized equation neglecting the nonlinear advection terms and obtains a sinusoidal velocity. In the second order, the nonlinear advection term appears as a forcing term for the equation upon averaging

$$\mu\nabla^2\langle \mathbf{u}^{(2)}\rangle_t - \boldsymbol{\nabla}\langle p^{(2)}\rangle_t = \mathbf{F} = \rho\langle \mathbf{u}^{(1)} \cdot \boldsymbol{\nabla}\mathbf{u}^{(1)}\rangle_t, \tag{20}$$

where $\langle\cdot\rangle_t$ is the average over the time period of the oscillating excitation and describes the steady average streaming motion. As can be seen from Eq. (20), the streaming motion is forced by the first-order velocity $\mathbf{u}^{(1)}$, which in totality is determined by its far-field potential part due to the bubble motion near a wall. In other words, once the potential flow due to a periodically oscillating bubble near a wall is computed, it can be used to obtain the streaming motion $\langle \mathbf{u}^{(2)}\rangle_t$, and thereby the stress $\tau_{\rm wall} = \mu(\partial\langle u^{(2)}\rangle_t/\partial z)$ at the wall $z = 0$ using the radial component of the streaming velocity. We also computed its vertical component using the continuity equation (was not there in Nyborg's article [93]), which allowed us to plot the streamlines of the axisymmetric toroidal vortex in the boundary layer region of the wall [Fig. 10(a)]. The analytical solution predicted 12.8 Pa for a free bubble of radius 1.6 μm, oscillating due to an acoustic excitation of 70 kPa and 3 MHz situated above the wall twice the bubble radius away, considerably reducing to 6 Pa for a coated bubble with properties estimated for Sonazoid [106]. We find that the axial extent of the axisymmetric toroidal vortex scales with the bubble height from the wall $l_{\rm vortex}/R_0 = h/(\sqrt{2}R_0)$ while its height scales with the Stokes boundary layer $\delta_{\rm bl}$.

### 2. Jetting of an oscillating bubble

The analysis above for microstreaming was performed perturbatively for a linearly oscillating bubble excited by relatively low amplitude acoustic excitation. Under higher excitation strengths, bubbles are well known to undergo large inertial cavitation. In the presence of a nearby rigid wall, a bubble after undergoing expansion under the negative phase of the excitation, breaks the symmetry and forms a jet directed to the boundary during the collapse phase. Due to the inertial nature of the cavitation dynamics, the nonspherical deformation of a cavitating bubble has often been simulated using a boundary element/integral method (BEM) solving a potential flow field around the bubble [107–109].

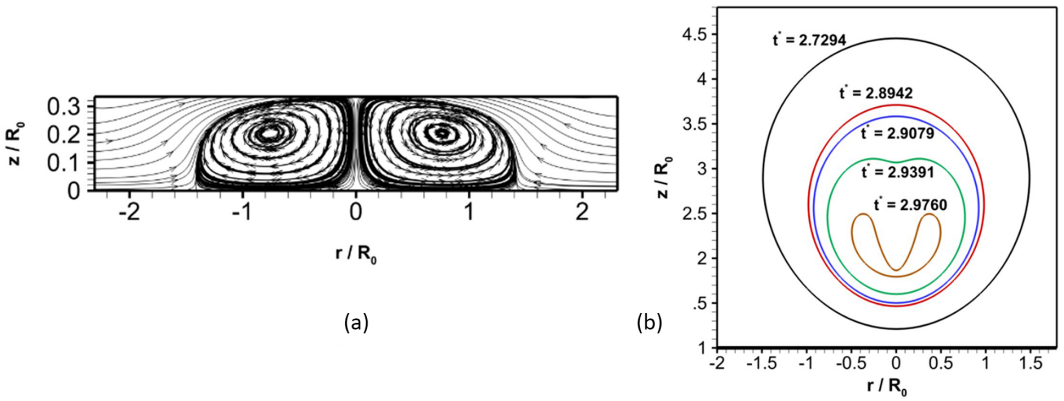


FIG. 10. (a) Microstreaming streamlines near the plane rigid wall due to an oscillating bubble of 1.6 μm radius situated above the wall twice the bubble radius away, excited by an acoustic wave of 70 kPa amplitude and 3 MHz frequency. (b) Collapse of a coated microbubble (Sonazoid) situated three times the radius away from the wall simulated using BEM. The excitation has an amplitude five times the ambient pressure and a frequency of 2 MHz. The interfacial rheological properties are those of Sonazoid (Sec. IV). $t'$ is time nondimensionalized using the bubble radius and ambient pressure.

We have studied the jetting of a coated bubble near a rigid wall using the boundary element method using our interfacial rheological model described above. The method and the results will be published in a future paper. Here, we briefly describe our effort. BEM solves the potential flow using the Green's function formulation of the flow. It relates the value of the velocity potential at any surface point of the bubble to two integrals over the bubble surface, one involving the velocity potential and the other involving its normal derivative, i.e., the normal velocity. Upon discretization of the axisymmetric bubble surface using line elements, and executing elementwise integration, one obtains a full matrix equation for the normal velocities at the bubble surface nodes, relating them to the potentials at those nodes. Those velocity potential values in turn are determined using Bernoulli's equation. To account for the presence of the encapsulating interface, Bernoulli's equation is modified using the appropriate pressure at the bubble surface [see, for instance, Eq. (6) modified for the EEM model (12)]. The bubble surface is updated with the computed normal velocity and the computation advances.

We found that without proper accounting for buckling, the negative (compressive) surface stress leads to essential numerical instability. It led us to develop a new criterion for buckling, with total surface stress becoming zero in contrast to only the surface tension becoming zero as per the Marmottant model, Eq. (13). It allowed computation of the jetting of a bubble [Fig. 10(b)].

## IX. FLUID MECHANICS RESEARCH INTO SUSPENSIONS AND EMULSIONS

I described how my journey into the world of bubbles and sound in medicine started with a chance meeting with folks in the field and it grew to be about 60% of my research portfolio (partly due to the availability of federal support that I greatly appreciate). But the other 40% strenuously remained tethered to the fundamental physics of fluid mechanics of drops, vesicles, red blood cells, and their suspensions and emulsions. It is a continuation of my postdoctoral work with Bill Schowalter on numerical simulation of inertial effects on drop dynamics in simple time-periodic linear flows [110–114]. I am extremely proud of my first PhD student, Xiaoyi Li, who won the 2009 Andrea Acrivos Award for the best dissertation in fluid dynamics from the American Physical Society. Through simulations, he demonstrated that micro-inertial effects in drop dynamics lead to unusual rheology of the emulsion, reversing the sign of the first and second normal stress differences in shear [115] and giving rise to negative normal stress elasticity in oscillating extensional flows

[116]. We investigated the effects of viscoelasticity on drop dynamics [117–122] and directly computed shear-induced gradient diffusivity in an emulsion of viscous drops [123–125] and a suspension of red blood cells. This part of my computational fluid dynamics research is driven by a desire to understand the fundamental physics behind the rheological phenomena in suspensions and emulsions. We have been continually developing a direct numerical simulation tool as a test bed to investigate these physical systems in search of interesting, unusual behaviors, which we then explain using analytical tools, e.g., one-dimensional models and perturbation methods.

## X. CONCLUDING REMARKS

Here, I presented a survey of our more than two-decade-old research on the dynamics of coated microbubbles used for various biomedical purposes such as contrast-enhanced ultrasound imaging, organ-level pressure monitoring using SHAPE, microbubble and ultrasound-assisted fracture healing, cancer therapy, and bone and cartilage tissue engineering. The work and my journey would not be possible without the help of a group of wonderful students. All of them have succeeded in their career pursuits and personal lives, a source of great pride and satisfaction for me. I consider them the primary deliverables of my academic research and scholarship effort.

Most of the results have already appeared in previous articles. The datasets generated and analyzed for others presented are available from the author on reasonable request.

## ACKNOWLEDGMENTS

K.S. acknowledges the work of his first postdoctoral scientist, currently Prof. Diman Chatterjee of IIT Madras (for starting his experimental research), and his students Pankaj Jain, Nishith Aggarwal, Peter Olapade, Priyesh Srivastava, Dr. Xiaoyi Li, Dr. Swarnajay Mukherjee, Dr. Rajesh Singh, Dr. Amit Katiyar, Dr. Shirshendu Paul, Dr. Mitra Aliabouzar, Dr. Lang Xia, Dr. Krishna Kumar, Dr. Nima Mobadersany, Dr. Jenna Osborne, Dr. Abhilash Malipeddi Reddy, Dr. Anik Tarafder, and Dr. Roozbeh Hassanzadeh Azami, as well as collaborations with Prof. Flemming Forsberg, Prof. John Eisenbrey, Prof. Sanku Mallik, and Prof. Grace Zhang. K.S. acknowledges partial support from NIH awards R01EB032333, R01GM114080 and NSF award 2037849.

The author declares no conflict of interest.

[1] A. Prosperetti, Bubble dynamics in oceanic ambient noise, in *Sea Surface Sound: Natural Mechanisms of Surface Generated Noise in the Ocean*, edited by B. R. Kerman (Springer Netherlands, Dordrecht, 1988), pp. 151–171.

[2] A. Prosperetti, Bubble-related ambient noise in the ocean, J. Acoust. Soc. Am. **84**, 1042 (1988).

[3] K. Sarkar and A. Prosperetti, Backscattering of underwater noise by bubble clouds, J. Acoust. Soc. Am. **93**, 3128 (1993).

[4] K. Sarkar and A. Prosperetti, Coherent and incoherent-scattering by oceanic bubbles, J. Acoust. Soc. Am. **96**, 332 (1994).

[5] K. Sarkar and A. Prosperetti, Effective boundary conditions for the Laplace equation with a rough boundary, Proc. R. Soc. London, Ser. A **451**, 425 (1995).

[6] K. Sarkar and A. Prosperetti, Effective boundary conditions for Stokes flow over a rough surface, J. Fluid Mech. **316**, 223 (1996).

[7] K. Sarkar, W. T. Shi, D. Chatterjee, and F. Forsberg, Characterization of ultrasound contrast microbubbles using in vitro experiments and viscous and viscoelastic interface models for encapsulation, J. Acoust. Soc. Am.**118**, 539 (2005).

[8] S. Paul, D. Russakow, T. Rodgers, K. Sarkar, M. Cochran, and M. A. Wheatley, Determination of the interfacial rheological properties of a poly(DL-lactic acid)-encapsulated contrast agent using in vitro attenuation and scattering, Ultrasound Med. Biol. **39**, 1277 (2013).
[9] R. Gramiak and P. M. Shah, Echocardiography of the aortic root, Invest. Radiol. **3**, 356 (1968).
[10] N. de Jong, A. Bouakaz, and P. Frinking, Basic acoustic properties of microbubbles, Echocardiography **19**, 229 (2002).
[11] P. S. Epstein and M. S. Plesset, On the stability of gas bubbles in liquid-gas solutions, J. Chem. Phys. **18**, 1505 (1950).
[12] K. Sarkar, A. Katiyar, and P. Jain, Growth and dissolution of an encapsulated contrast microbubble, Ultrasound Med. Biol. **35**, 1385 (2009).
[13] A. Katiyar, K. Sarkar, and P. Jain, Effects of encapsulation elasticity on the stability of an encapsulated microbubble, J. Colloid Interface Sci. **336**, 519 (2009).
[14] A. Katiyar and K. Sarkar, Stability analysis of an encapsulated microbubble against gas diffusion, J. Colloid Interface Sci. **343**, 42 (2010).
[15] K. Kooiman, H. J. Vos, M. Versluis, and N. de Jong, Acoustic behavior of microbubbles and implications for drug delivery, Adv. Drug Delivery Rev. **72**, 28 (2014).
[16] B. B. Goldberg, J. S. Raichlen, and F. Forsberg, *Ultrasound Contrast Agents: Basic Principles and Clinical Applications,* 2nd ed. (Martin Dunitz, London, 2001), p. 440.
[17] K. Ferrara, R. Pollard, and M. Borden, Ultrasound microbubble contrast agents: Fundamentals and application to gene and drug delivery, Annu. Rev. Biomed. Eng. **9**, 415 (2007).
[18] N. de Jong, F. J. Ten Cate, C. T. Lancée, J. R. T. C. Roelandt, and N. Bom, Principles and recent developments in ultrasound contrast agents, Ultrasonics **29**, 324 (1991).
[19] N. de Jong, L. Hoff, T. Skotland, and N. Bom, Absorption and scatter of encapsulated gas filled microspheres: Theoretical considerations and some measurements, Ultrasonics **30**, 95 (1992).
[20] N. de Jong and L. Hoff, Ultrasound scattering properties of albunex microspheres, Ultrasonics **31**, 175 (1993).
[21] N. de Jong, Improvements in ultrasound contrast agents, IEEE Eng. Med. Biol. Mag. **15**, 72 (1996).
[22] A. Bouakaz, N. De Jong, and C. Cachard, Standard properties of ultrasound contrast agents, Ultrasound Med. Biol. **24**, 469 (1998).
[23] N. de Jong, R. Cornet, and C. T. Lancee, Higher harmonics of vibrating gas-filled microspheres. Part one. Simulations, Ultrasonics **32**, 447 (1994).
[24] J. S. Allen, D. J. May, and K. W. Ferrara, Dynamics of therapeutic ultrasound contrast agents, Ultrasound Med. Biol. **28**, 805 (2002).
[25] K. E. Morgan, J. S. Allen, P. A. Dayton, J. E. Chomas, A. L. Klibaov, and K. W. Ferrara, Experimental and theoretical evaluation of microbubble behavior: Effect of transmitted phase and bubble size, IEEE Trans. Ultrason. Ferroelectr. Freq. Control **47**, 1494 (2000).
[26] D. B. Khismatullin and A. Nadim, Radial oscillations of encapsulated microbubbles in viscoelastic liquids, Phys. Fluids **14**, 3534 (2002).
[27] C. C. Church, The effects of an elastic solid-surface layer on the radial pulsations of gas-bubbles, J. Acoust. Soc. Am. **97**, 1510 (1995).
[28] J. M. Gorce, M. Arditi, and M. Schneider, Influence of bubble size distribution on the echogenicity of ultrasound contrast agents: A study of SonoVue, Invest. Radiol. **35**, 661 (2000).
[29] L. Hoff, P. C. Sontum, and J. M. Hovem, Oscillations of polymeric microbubbles: Effect of the encapsulating shell, J. Acoust. Soc. Am. **107**, 2272 (2000).
[30] D. Chatterjee and K. Sarkar, A Newtonian rheological model for the interface of microbubble contrast agents, Ultrasound Med. Biol. **29**, 1749 (2003).
[31] S. Paul, A. Katiyar, K. Sarkar, D. Chatterjee, W. T. Shi, and F. Forsberg, Material characterization of the encapsulation of an ultrasound contrast microbubble and its subharmonic response: Strain-softening interfacial elasticity model, J. Acoust. Soc. Am. **127**, 3846 (2010).
[32] P. Marmottant, S. van der Meer, M. Emmer, M. Versluis, N. de Jong, S. Hilgenfeldt, and D. Lohse, A model for large amplitude oscillations of coated bubbles accounting for buckling and rupture, J. Acoust. Soc. Am. **118**, 3499 (2005).

[33] T. Faez, M. Emmer, K. Kooiman, M. Versluis, A. van der Steen, and N. de Jong, 20 years of ultrasound contrast agent modeling, IEEE Trans. Ultrason. Ferroelectr. Freq. Control **60**, 7 (2013).
[34] D. Chatterjee, K. Sarkar, P. Jain, and N. E. Schreppler, On the suitability of broadband attenuation measurement for characterizing contrast microbubbles, Ultrasound Med. Biol. **31**, 781 (2005).
[35] P. H. Chang, K. K. Shun, S.-J. Wu, and H. B. Levene, Second-harmonic imaging and harmonic Doppler measurements with Albunex, IEEE Trans. Ultrason. Ferroelectr. Freq. Control **42**, 1020 (1995).
[36] P. H. Chang, K. K. Shung, and H. B. Levene, Quantitative measurements of second harmonic Doppler using ultrasound contrast agents, Ultrasound Med. Biol. **22**, 1205 (1996).
[37] F. Forsberg, J. B. Liu, W. T. Shi, J. Furuse, M. Shimizu, and B. B. Goldberg, In vivo pressure estimation using subharmonic contrast microbubble signals: proof of concept, IEEE Trans. Ultrason Ferroelectr. Freq. Control **52**, 581 (2005).
[38] A. Katiyar, K. Sarkar, and F. Forsberg, Modeling subharmonic response from contrast microbubbles as a function of ambient static pressure, J. Acoust. Soc. Am. **129**, 2325 (2011).
[39] R. H. Azami, F. Forsberg, J. R. Eisenbrey, and K. Sarkar, Acoustic response and ambient pressure sensitivity characterization of SonoVue for noninvasive pressure estimation, J. Acoust. Soc. Am. **155**, 2636 (2024).
[40] R. H. Azami, F. Forsberg, J. R. Eisenbrey, and K. Sarkar, Ambient pressure sensitivity of the subharmonic response of coated microbubbles: Effects of acoustic excitation parameters, Ultrasound Med. Biol.**49**, 1550 (2023).
[41] L. Xia, T. M. Porter, and K. Sarkar, Interpreting attenuation at different excitation amplitudes to estimate strain-dependent interfacial rheological properties of lipid-coated monodisperse microbubbles, J. Acoust. Soc. Am. **138**, 3994 (2015).
[42] A. A. Doinikov and P. A. Dayton, Maxwell rheological model for lipid-shelled ultrasound microbubble contrast agents, J. Acoust. Soc. Am. **121**, 3331 (2007).
[43] A. A. Doinikov, J. F. Haac, and P. A. Dayton, Modeling of nonlinear viscous stress in encapsulating shells of lipid-coated contrast agent microbubbles, Ultrasonics **49**, 269 (2009).
[44] S. M. van der Meer, B. Dollet, M. M. Voormolen, C. T. Chin, A. Bouakaz, N. de Jong, M. Versluis, and D. Lohse, Microbubble spectroscopy of ultrasound contrast agents, J. Acoust. Soc. Am.**121**, 648 (2007).
[45] K. Tsiglifis and N. A. Pelekasis, Nonlinear radial oscillations of encapsulated microbubbles subject to ultrasound: The effect of membrane constitutive law, J. Acoust. Soc. Am. **123**, 4059 (2008).
[46] E. Stride, The influence of surface adsorption on microbubble dynamics, Philos. Trans. R. Soc. A **366**, 2103 (2008).
[47] N. de Jong, M. Emmer, C. T. Chin, A. Bouakaz, F. Mastik, D. Lohse, and M. Versluis, "Compression-only" behavior of phospholipid-coated contrast bubbles, Ultrasound Med. Biol.**33**, 653 (2007).
[48] K. N. Kumar and K. Sarkar, Effects of ambient hydrostatic pressure on the material properties of the encapsulation of an ultrasound contrast microbubble, J. Acoust. Soc. Am. **138**, 624 (2015).
[49] K. N. Kumar and K. Sarkar, Interfacial rheological properties of contrast microbubble targesar P as a function of ambient pressure, Ultrasound Med Biol. **42**, 1010 (2016).
[50] R. H. Azami, M. Aliabouzar, J. Osborn, K. N. Kumar, F. Forsberg, J. R. Eisenbrey, S. Mallik, and K. Sarkar, Material properties, dissolution and time evolution of PEGylated lipid-shelled microbubbles: Effects of the PEG hydrophilic chain configurations, Ultrasound Med. Biol. **48**, 1720 (2022).
[51] M. A. Borden and M. L. Longo, Dissolution behavior of lipid monolayer-coated, air-filled microbubbles: Effect of lipid hydrophobic chain length, Langmuir **18**, 9225 (2002).
[52] M. Aliabouzar, X. Lu, O. D. Kripfgans, J. B. Fowlkes, and M. L. Fabiilli, Acoustic droplet vaporization in acoustically responsive scaffolds: Effects of frequency of excitation, volume fraction and threshold determination method, Ultrasound Med. Biol. **45**, 3246 (2019).
[53] J. Sijl, B. Dollet, M. Overvelde, V. Garbin, T. Rozendal, N. de Jong, D. Lohse, and M. Versluis, Subharmonic behavior of phospholipid-coated ultrasound contrast agent microbubbles, J. Acoust. Soc. Am. **128**, 3239 (2010).
[54] J. F. Guan and T. J. Matula, Using light scattering to measure the response of individual ultrasound contrast microbubbles subjected to pulsed ultrasound *in vitro*, J. Acoust. Soc. Am. **116**, 2832 (2004).

[55] T. Segers, E. Gaud, M. Versluis, and P. Frinking, High-precision acoustic measurements of the nonlinear dilatational elasticity of phospholipid coated monodisperse microbubbles, Soft Matter **14**, 9550 (2018).
[56] T. Segers, L. de Rond, N. de Jong, M. Borden, and M. Versluis, Stability of monodisperse phospholipid-coated microbubbles formed by flow-focusing at high production rates, Langmuir **32**, 3937 (2016).
[57] A. Kabalnov, D. Klein, T. Pelura, E. Schutt, and J. Weers, Dissolution of multicomponent microbubbles in the bloodstream: 1, Theory. Ultrasound Med. Biol. **24**, 739 (1998).
[58] A. Kabalnov, J. Bradley, S. Flaim, D. Klein, T. Pelura, B. Peters, S. Otto, J. Reynolds, E. Schutt, and J. Weers, Dissolution of multicomponent microbubbles in the bloodstream: 2. Experiment, Ultrasound Med. Biol. **24**, 751 (1998).
[59] D. Chatterjee, P. Jain, and K. Sarkar, Ultrasound-mediated destruction of contrast microbubbles used for medical imaging and drug delivery, Phys. Fluids **17**, 100603 (2005).
[60] M. Blank and V. K. La Mer, The energy barrier for monolayer penetration, in *Retardation of Evaporation by Monolayers*, edited by V. K. La Mer (Academic, New York, 1962), pp. 59–66.
[61] G. Pu, M. A. Borden, and M. L. Longo, Collapse and shedding transitions in binary lipid monolayers coating microbubbles, Langmuir **22**, 2993 (2006).
[62] J. J. Kwan and M. A. Borden, Lipid monolayer collapse and microbubble stability, Adv. Colloid Interface Sci. **183-184**, 82 (2012).
[63] Y. Itai and O. Matsui, Blood flow and liver imaging, Radiology **202**, 306 (1997).
[64] P. C. Pieters, W. J. Miller, and J. H. DeMeo, Evaluation of the portal venous system: Complementary roles of invasive and noninvasive imaging strategies, Radiographics **17**, 879 (1997).
[65] G. Garcia-Tsao, R. J. Groszmann, R. L. Fisher, H. O. Conn, C. E. Atterbury, and M. Glickman, Portal pressure, presence of gastroesophageal varices and variceal bleeding, Hepatology **5**, 419 (1985).
[66] E. A. Tsochatzis, J. Bosch, and A. K. Burroughs, Liver cirrhosis, Lancet **383**, 1749 (2014).
[67] M. Kudo *et al.*, Diagnostic accuracy of imaging for liver cirrhosis compared to histologically proven liver cirrhosis: A multicenter collaborative study, Intervirology **51**, 17 (2008).
[68] A. Nohria, S. W. Tsang, J. C. Fang, E. F. Lewis, J. A. Jarcho, G. H. Mudge, and L. W. Stevenson, Clinical assessment identifies hemodynamic profiles that predict outcomes in patients admitted with heart failure, J. Am. Coll. Cardiol. **41**, 1797 (2003).
[69] M. C. Fishbein and J. Kobashigawa, Biopsy-negative cardiac transplant rejection: Etiology, diagnosis, and therapy, Curr. Opin. Cardiol. **19**, 166 (2004).
[70] S. D. Solomon and L. W. Stevenson, Recalibrating the barometer, Circulation **119**, 13 (2009).
[71] A. K. Reddy, G. E. Taffet, S. Madala, L. H. Michael, M. L. Entman, and C. J. Hartley, Noninvasive blood pressure measurement in mice using pulsed Doppler ultrasound, Ultrasound Med. Biol. **29**, 379 (2003).
[72] A. L. Strauss, F. J. Roth, and H. Rieger, Noninvasive assessment of pressure gradients across iliac artery stenoses: Duplex and catheter correlative study, J. Ultrasound Med. **12**, 17 (1993).
[73] W. T. Shi, F. Forsberg, J. S. Raichlen, L. Needleman, and B. B. Goldberg, Pressure dependence of subharmonic signals from contrast microbubbles, Ultrasound Med. Biol. **25**, 275 (1999).
[74] L. Leodore, F. Forsberg, and W. T. Shi, *In vitro* pressure estimation obtained from subharmonic contrast microbubble signals, in *IEEE Ultrasonics Symposium Proceedings* (2007), pp. 2207–2210.
[75] J. K. Dave, V. G. Halldorsdottir, J. T. Eisenbrey, J. S. Raichlen, J.-B. Liu, M. E. McDonald, K. Dickie, S. Wang, C. Leung, and F. Forsberg, Noninvasive LV pressure estimation using subharmonic emissions from microbubbles, JACC Cardiovasc Imaging **5**, 87 (2012).
[76] V. G. Halldorsdottir, J. K. Dave, J. R. Eisenbrey, P. Machado, H. Zhao, J. B. Liu, D. A. Merton, and F. Forsberg, Subharmonic aided pressure estimation for monitoring interstitial fluid pressure in tumours—in vitro and in vivo proof of concept, Ultrasonics **54**, 1938 (2014).
[77] V. G. Halldorsdottir, J. K. Dave, A. Marshall, A. I. Forsberg, T. B. Fox, J. R. Eisenbrey, P. Machado, J.-B. Liu, D. A. Merton, and F. Forsberg, Subharmonic-aided pressure estimation for monitoring interstitial fluid pressure in tumors: Calibration and treatment with paclitaxel in breast cancer xenografts, Ultrasound Med. Biol. **43**, 1401 (2017).
[78] I. Gupta *et al.*, Diagnosing portal hypertension with noninvasive subharmonic pressure estimates from a US contrast agent, Radiology **298**, 104 (2021).

[79] J. R. Eisenbrey *et al.*, Chronic liver disease: Noninvasive subharmonic aided pressure estimation of hepatic venous pressure gradient, Radiology **268**, 581 (2013).
[80] J. K. Dave *et al.*, Investigating the efficacy of subharmonic aided pressure estimation for portal vein pressures and portal hypertension monitoring, Ultrasound Med. Biol. **38**, 1784 (2012).
[81] A. Prosperetti, Subharmonics and ultraharmonics in forced-oscillations of weakly nonlinear-systems, Am. J. Phys. **44**, 548 (1976).
[82] A. Katiyar and K. Sarkar, Excitation threshold for subharmonic generation from contrast microbubbles, J. Acoust. Soc. Am. **130**, 3137 (2011).
[83] A. Katiyar and K. Sarkar, Effects of encapsulation damping on the excitation threshold for subharmonic generation from contrast microbubbles, J. Acoust. Soc. Am. **132**, 3576 (2012).
[84] P. J. Frinking, J. Brochot, and M. Arditi, Subharmonic scattering of phospholipid-shell microbubbles at low acoustic pressure amplitudes, IEEE Trans. Ultrason. Ferroelectr. Freq. Control **57**, 1762 (2010).
[85] A. Katiyar, R. L. Duncan, and K. Sarkar, Ultrasound stimulation increases proliferation of MC3T3-E1 preosteoblast-like cells, J. Ther. Ultrasound **2**, 1 (2014).
[86] A. Katiyar, J. Osborn, M. DasBanerjee, L. G. Zhang, K. Sarkar, and K. Pada Sarker, Inhibition of human breast cancer cell proliferation by low-intensity ultrasound stimulation, J. Ultrasound Med. **39**, 2043 (2020).
[87] X. Zhou, N. J. Castro, W. Zhu, H. Cui, M. Aliabouzar, K. Sarkar, and L. G. Zhang, Improved human bone marrow mesenchymal stem cell osteogenesis in 3D bioprinted tissue scaffolds with low intensity pulsed ultrasound stimulation, Sci. Rep. **6**, 12 (2016).
[88] M. Aliabouzar, L. G. Zhang, and K. Sarkar, Lipid coated microbubbles and low intensity pulsed ultrasound enhance chondrogenesis of human mesenchymal stem cells in 3D printed scaffolds, Sci. Rep. **6**, 37728 (2016).
[89] M. Aliabouzar, S.-j. Lee, X. Zhou, G. L. Zhang, and K. Sarkar, Effects of scaffold microstructure and low intensity pulsed ultrasound on chondrogenic differentiation of human mesenchymal stem cells, Biotechnol. Bioeng. **115**, 495 (2018).
[90] M. Aliabouzar, G. L. Zhang, and K. Sarkar, Acoustic and mechanical characterization of 3D-printed scaffolds for tissue engineering applications, Biomed. Mater. **13**, 055013 (2018).
[91] J. Osborn, M. Aliabouzar, X. Zhou, R. Rao, L. G. Zhang, and K. Sarkar, Lipid-coated microbubbles: Enhanced osteogenic differentiation of human mesenchymal stem cells using microbubbles and low intensity pulsed ultrasound on 3D printed scaffolds (Adv. Biosys. 2/2019), Adv. Biosyst. **3**, 1970021 (2019).
[92] W. L. Nyborg, Acoustic streaming due to attenuated plane waves, J. Acoust. Soc. Am. **25**, 68 (1953).
[93] W. L. Nyborg, Acoustic streaming near a boundary, J. Acoust. Soc. Am. **30**, 329 (1958).
[94] P. Tho, R. Manasseh, and A. Ooi, Cavitation microstreaming patterns in single and multiple bubble systems, J. Fluid Mech. **576**, 191 (2007).
[95] N. Riley, Steady streaming, Annu. Rev. Fluid Mech. **33**, 43 (2001).
[96] J. A. Rooney, Hemolysis near an ultrasonically pulsating gas bubble, Science **169**, 869 (1970).
[97] P. Marmottant and S. Hilgenfeldt, Controlled vesicle deformation and lysis by single oscillating bubbles, Nature (London) **423**, 153 (2003).
[98] A. Pommella, N. J. Brooks, J. M. Seddon, and V. Garbin, Selective flow-induced vesicle rupture to sort by membrane mechanical properties, Sci. Rep. **5**, 13163 (2015).
[99] Z. Fan, R. E. Kumon, and C. X. Deng, Mechanisms of microbubble-facilitated sonoporation for drug and gene delivery, Ther. Delivery **5**, 467 (2014).
[100] I. Lentacker, S. C. De Smedt, and N. N. Sanders, Drug loaded microbubble design for ultrasound triggered delivery, Soft Matter **5**, 2161 (2009).
[101] C. Wang, S. V. Jalikop, and S. Hilgenfeldt, Efficient manipulation of microparticles in bubble streaming flows, Biomicrofluidics **6**, 11 (2012).
[102] X. Liu and J. Wu, Acoustic microstreaming around an isolated encapsulated microbubble, J. Acoust. Soc. Am. **125**, 1319 (2009).

[103] S. Orbay *et al.*, Mixing high-viscosity fluids via acoustically driven bubbles, J. Micromech. Microeng. **27**, 015008 (2016).
[104] P. J. Westervelt, The theory of steady rotational flow generated by a sound field, J. Acoust. Soc. Am. **25**, 60 (1953).
[105] J. Lighthill, Acoustic streaming, J. Sound Vib. **61**, 391 (1978).
[106] N. Mobadersany and K. Sarkar, Acoustic microstreaming near a plane wall due to a pulsating free or coated bubble: Velocity, vorticity and closed streamlines, J. Fluid Mech. **875**, 781 (2019).
[107] M. L. Calvisi, O. Lindau, J. R. Blake, and A. J. Szeri, Shape stability and violent collapse of microbubbles in acoustic traveling waves, Phys. Fluids **19**, 047101 (2007).
[108] Q. Wang and J. Blake, Non-spherical bubble dynamics in a compressible liquid. Part 1. Travelling acoustic wave, J. Fluid Mech. **659**, 191 (2010).
[109] Q. Wang and J. Blake, Non-spherical bubble dynamics in a compressible liquid. Part 2. Acoustic standing wave, J. Fluid Mech. **679**, 559 (2011).
[110] K. Sarkar and W. R. Schowalter, Deformation of a two-dimensional viscoelastic drop at non-zero Reynolds number in time-periodic extensional flows, J. Non-Newtonian Fluid Mech. **95**, 315 (2000).
[111] K. Sarkar and W. R. Schowalter, Deformation of a two-dimensional drop at non-zero Reynolds number in time-periodic extensional flows: Numerical simulation, J. Fluid Mech. **436**, 177 (2001).
[112] K. Sarkar and W. R. Schowalter, Deformation of a two-dimensional viscous drop in time-periodic extensional flows: Analytical treatment, J. Fluid Mech. **436**, 207 (2001).
[113] X. Li and K. Sarkar, Drop dynamics in an oscillating extensional flow at finite Reynolds numbers, Phys. Fluids **17**, 027103 (2005).
[114] X. Y. Li and K. Sarkar, Front tracking simulation of deformation and buckling instability of a liquid capsule enclosed by an elastic membrane, J. Comput. Phys. **227**, 4998 (2008).
[115] X. Y. Li and K. Sarkar, Effects of inertia on the rheology of a dilute emulsion of drops in shear, J. Rheol. **49**, 1377 (2005).
[116] X. Li and K. Sarkar, Negative normal stress elasticity of emulsions of viscous drops at finite inertia, Phys. Rev. Lett. **95**, 256001 (2005).
[117] N. Aggarwal and K. Sarkar, Deformation and breakup of a viscoelastic drop in a Newtonian matrix under steady shear, J. Fluid Mech. **584**, 1 (2007).
[118] N. Aggarwal and K. Sarkar, Effects of matrix viscoelasticity on viscous and viscoelastic drop deformation in a shear flow, J. Fluid Mech. **601**, 63 (2008).
[119] N. Aggarwal and K. Sarkar, Rheology of an emulsion of viscoelastic drops in steady shear, J. Non-Newtonian Fluid Mech. **150**, 19 (2008).
[120] S. Mukherjee and K. Sarkar, Viscoelastic drop falling through a viscous medium, Phys. Fluids **23**, 013101 (2011).
[121] S. Mukherjee and K. Sarkar, Lateral migration of a viscoelastic drop in a Newtonian fluid in a shear flow near a wall, Phys. Fluids **26**, 103102 (2014).
[122] A. Tarafder, A. R. Malipeddi, and K. Sarkar, Pair interactions between viscous drops in a viscoelastic matrix in free shear: Transition from passing to tumbling trajectories, J. Rheol. **66**, 571 (2022).
[123] A. R. Malipeddi and K. Sarkar, Shear-induced collective diffusivity down a concentration gradient in a viscous emulsion of drops, J. Fluid Mech. **868**, 5 (2019).
[124] A. R. Malipeddi and K. Sarkar, Collective diffusivity in a sheared viscous emulsion: Effects of viscosity ratio, Phys. Rev. Fluids **4**, 093603 (2019).
[125] A. R. Malipeddi and K. Sarkar, Shear-induced gradient diffusivity of a red blood cell suspension: Effects of cell dynamics from tumbling to tank-treading, Soft Matter **17**, 8523 (2021).